SEA SURFACE RADAR BACKSCATTERING CROSS-SECTION IN KA-BAND

Yury Yu. Yurovsky[1], Vladimir N. Kudryavstev[1,2], Semyon A. Grodsky[3], Bertrand Chapron[4]

[1]Marine Hydrophysical Institute RAS (MHI RAS),
Kapitanskaya 2, Sevastopol 299011, Russia, Email: yyyurovsky@gmail.com
[2]Russian State Hydrometeorological University (RSHU),
Malookhtinsky 98, St. Petersburg 195196, Russia, Email: kudr@rshu.ru
[3]Department of Atmospheric and Oceanic Science,
University of Maryland, College Park, USA, Email: senya@umd.edu
[4]Institut Français de Recherche pour l'Exploitation de la Mer (IFREMER)
Brest, France, Email: Bertrand.Chapron@ifremer.fr

KEYWORDS: radar, backscattering, sea, surface, Ka-band

ABSTARCT: An empirical model of the Ka-band radar backscattering cross-section of the sea surface is presented based on the field measurements. Doppler dual-polarized (VV and HH) radar is used in the experiments to estimate normalized radar cross-section (NRCS) of the sea surface. Radar incidence angle (the angle between vertical and look direction) was varied from 0º to 70º, while radar azimuth relative to the wind was changed from 0º (up-wind) to 180º (down-wind). The range of observed wind speed is from 3 to 20 m/s. Special calibration procedures are made to obtain absolute NRCS values and to correct observed data for the finite radar antenna pattern beam width. Three standard variables are chosen to parametrize observed NRCS in log units (dB): incidence angle, azimuth and wind speed. The fitting function is fourth-order polynomial of incidence angle and logarithm of wind speed, expanded in Fourier series of azimuth angle (first two terms). The non-linear fitting is done iteratively by minimization of the difference between expected NRCS (the convolution of the model with the measured radar footprint) and actually measured NRCS. Obtained empirical Ka-band model is compared to the published Ka-band and Ku-band data and models. It is shown that our Ka-band NRCS are generally quite close to that in Ku-band, however important differences are indicated. Particularly, although non-polarized return increases with incidence angle, Bragg return is more noticeable in Ka-band than in Ku-band. This effect is explained by short-scale wave breaking and parasitic ripple generation.

1. INTRODUCTION

The global tendency in recent and planned satellite radar missions is shortening of operating wavelength. This lets to improve spatial data resolution with decrease in weight, size and cost of the instrument. The first spaceborne Ka-band altimeter AltiKa (Vincent et al., 2006) is launched in 2013 and demonstrates a three times better accuracy as compared to traditional Ku-band sensors. The planned for 2019 Ka-band interferometer KaRIN is expected to provide the first radar mesoscale ocean survey (Durand et al., 2010). Today the Ka-band airborne SAR (Doerry et al., 2005) already provides the spatial resolution of about 10 cm that is much better than in C- or X-bands.

In this context the Ka-band backscattering from the sea surface is of special interest, but not well studied yet. The first tabulated model for the sea surface cross-section in Ka-band has been proposed by Masuko et al. (1986) for VV and HH polarizations from airborne measurements. Later this model has been revisited and partly represented (only VV and fixed incidence angles) in an analytical form by Nekrasov and Hoogeboom (2005). However, a noticeable deviation of about 5 – 6 dB from the Masuko et al. (1986) data has been reported by Walsh et al. (1998), Vandemark et al. (2004), Tanelli et al. (2006) at near-nadir incidence angles. This discrepancy has been attributed to the imprecise calibration that was made in (Masuko et al., 1986). At moderate incidence angles the published Ka-band measurements are even more rare (Giovanangeli et al., 1991; Plant et al., 1994; Boisot et al., 2015) and also demonstrate the cross-sections exceeding the Masuko et al. (1986) model.

In this message an empirical model of the sea surface Ka-band radar cross-section is presented based on the field measurements carried out at the Black Sea research platform in 2009 – 2015. The developed model (KaDPM) is compared to the known published Ka- and Ku-band data and models.

2. MEASUREMENTS

2.1 Experiment and Equipment

The measurements are conducted at the Marine Hydrophysical Institute Research platform located in the Black Sea abeam of cape Kikeneiz (44°23’35” N, 33°59’04” E). The platform is moored 600 m offshore at 25 m – 30 m depth (Figure 1).

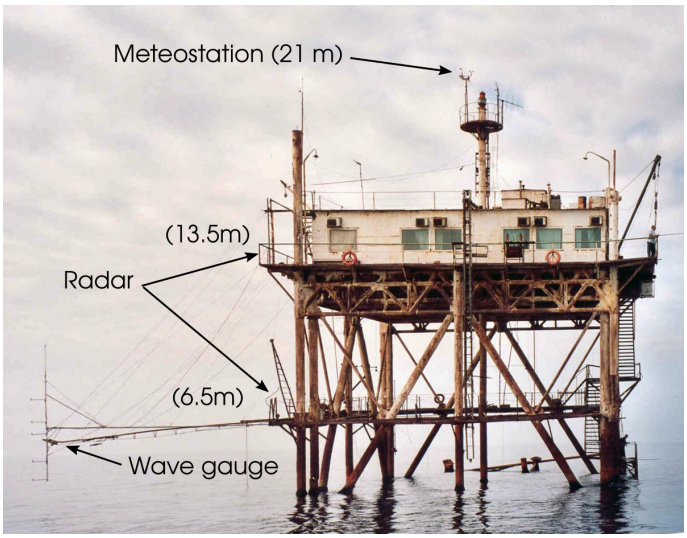

Figure 1. The Black sea research platform of Marine Hydrophysical Institute.

A Ka-band (37.5 GHz) continuous wave Doppler radar was used for the radar measurements. The radar has two conical horn antennae for transmitting and receiving. The transmitter built on the Gunn oscillator operates at slant polarization mode (polarization plane is inclined by 45° from the radar incidence plane), thus vertical and horizontal components are radiated simultaneously. The receiver has two separate vertical and horizontal channels. This hybrid radar design does not allow to discriminate between co-polarized and cross-polarized signals, but at wind speed below 25 m/s the cross-polarized backscatter is much lower than the co-polarized signals (Mouche and Chapron, 2015) and thus can be ignored.

Meteoparameters are measured using commercial weather station Davis Vantage Pro2 6152. The wind speed and direction, air temperature, pressure, and humidity at 21 m height and sea water temperature at 3 m depth were continuously monitored during radar acquisitions. Wave information is obtained using a wire wave gauge. Neutral wind speed at 10 m, U , is computed from the meteorological observations and the near surface water temperature using the COARE3.0 algorithm (Fairall et al., 2003).

2.2 Radar Calibration

The power of the signal backscattered from a stand-alone point-like target is determined by the radar equation $p = CGR^{-4}\sigma_t$, where C is the calibration constant, G is the two-way radar pattern in the direction of the target, R is the distance to the target, σ_t is the radar cross-section (RCS) of the target. A few metal targets (trihedral corner reflectors and spheres of different sizes) are used to determine radar calibration constant, C , and estimate the two-way patterns.

The sea surface is a distributed target, thus the backscattered power is integrated over the radar footprint:

$$p = CR_0^{-4}\int G(\mathbf{x})\sigma(\mathbf{x})R(\mathbf{x})^{-4}R_0^4 \mathrm{d}\mathbf{x} = CR_0^{-4}\sigma_e\,, \tag{1}$$

where $\mathbf{x}$ is the coordinates in the sea surface plane, $\sigma(\mathbf{x})$ is the local sea surface normalized RCS (NRCS), $G(\mathbf{x})$ is the two-way pattern in the direction from the radar to the integration point on the surface, $R(\mathbf{x})$ is the distance from radar to the integration point, R_0 is the slant range along radar principal axis, and σ_e is the effective RCS of the spatially distributed sea surface target.

The measured NRCS of the distributed sea surface target is defined as the ratio of effective RCS and effective radar footprint,

$$\sigma_e = pR_0^4C^{-1}\left\{\int G(\mathbf{x})R_0^4R(\mathbf{x})^{-4}\mathrm{d}\mathbf{x}\right\}^{-1}. \tag{2}$$

Radar internal noise prevents measurements at calm winds and/or low grazing angles, when power backscattered from the sea surface is low. The equivalent noise NRCS estimated from the signal of radar directed into the sky is subtracted from the measured NRCS.

2.3 Data Set

The acquisition time and radar look geometry were selected manually depending on wind and wave conditions. Each record was split into 5 min fragments (data samples). The total number of data samples is about 1500. Depending on desired incidence angle, θ, the radar is installed on upper or lower deck of the platform. The upper deck installation (13.5 m height) is used for incidence angles less than 45°, while the bottom installation (6.5 m height) is used for incidence angles more than 45°. In both cases the far field approximation is applicable.

Assuming that the NRCS is symmetrical relative to the wind direction, the data are folded in the azimuth range. Most of the collected data correspond to moderate and high ($45^\circ < \theta < 70^\circ$) incidence angles, while the near nadir data ($\theta < 30^\circ$) are sparse. Observed wind speed varies from 3 m/s to 18 m/s with more frequent occurrence of 5 m/s to 11 m/s winds. There are three typical wind directions at the platform location: easterly, southwesterly, and northerly. The latter is removed from analyzed data because it corresponds to offshore winds and short (~1 km) wave fetches. For easterly or southwesterly winds, the wave fetch is determined by the size of synoptic systems and can reach a few hundred kilometers. Our analysis focuses on wave/wind conditions typical for the open ocean. In addition, we also exclude cases of the swell-dominated sea. Swell-induced radar backscattering modulations, which may significantly affect the mean radar signal, are out of the scope of this study.

An examples of NRCS as a function of θ, ϕ, and U for cases with rather good statistics are shown in the Figure 2. The antenna pattern impact on measured NRCS is clearly seen at near-nadir θ, where NRCS for VV polarization is higher than for HH polarization, while they must be the same due to the specular reflections dominating at low incidence angles (Figure 2a-c).

In contrast to the incidence angle, the azimuth dependence of measured NRCS is not strongly affected by the antenna pattern, and "true" NRCS azimuthal features can be directly inferred from measured NRCS. At moderate incidence angles ($\theta = 45^\circ$, Figure 2e) the azimuth dependence demonstrates the expected behavior with crosswind minimum and upwind backscattering stronger than downwind backscattering. At lower incidence angles ($\theta = 32^\circ$, Figure 2d), the upwind to downwind difference vanishes (if not reverts) demonstrating that downwind wave slopes may be "rougher". At high incidence angles ($\theta = 70^\circ$, Figure 2f), the azimuth distribution becomes unimodal, with well-expressed upwind maximum and a minimum in the downwind direction, which is even lower than crosswind NRCS.

The wind dependencies of measured NRCS in general follow the power law (Figure 2g-i). However, some evidences of saturation are seen at rather strong winds, $U > 15$ m/s (Figure 2h).

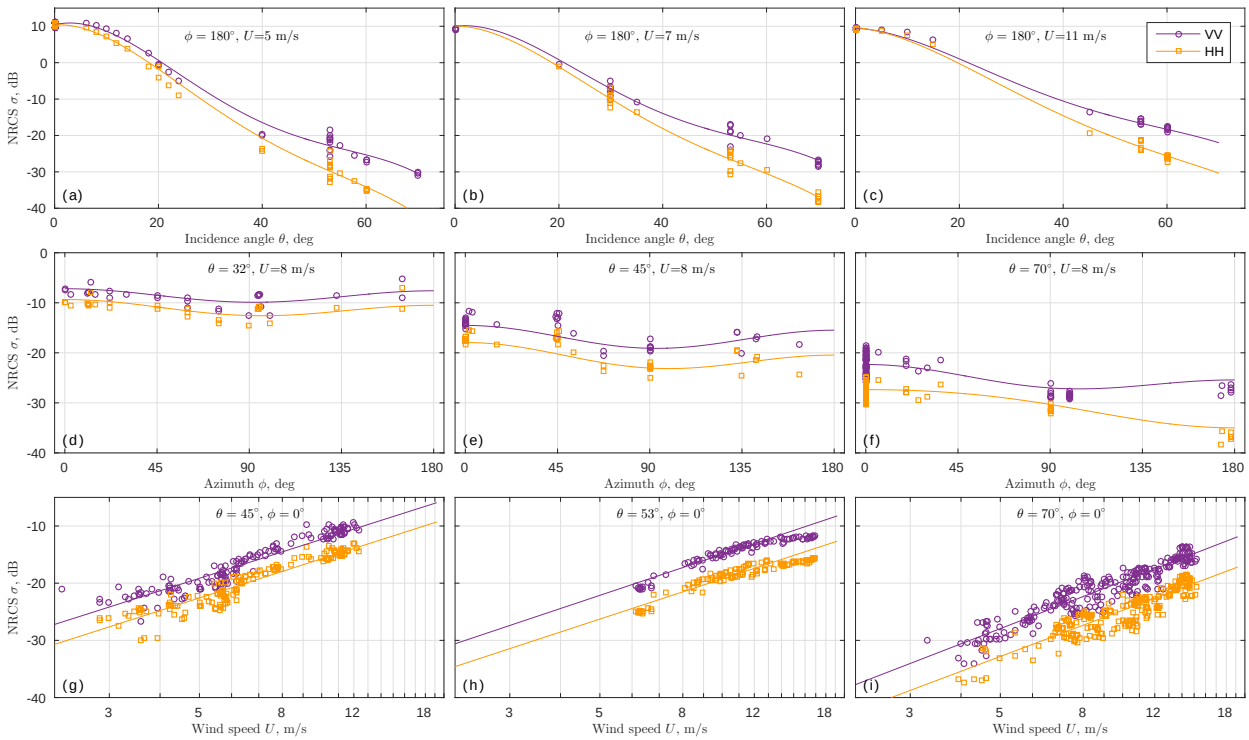

Figure 2. Measured NRCS versus (a,b,c) incidence angle, (d,e,f) azimuth, and (g,h,i) wind speed. Solid lines are the best data fit in form of (6).

3. RESULTS

3.1 Data Fitting

The effective NRCS, σ_e, measured at a given wind speed, U, nominal incidence angle, θ_0, and azimuth, ϕ_0, is a convolution of the true sea surface NRCS, σ, and the radar footprint, G:

$$\sigma_e(\theta_0,\phi_0,U) = \frac{\int G(\mathbf{x})R(\mathbf{x})^{-4}\sigma(\mathbf{x},U)d\mathbf{x}}{\int G(\mathbf{x})R(\mathbf{x})^{-4}d\mathbf{x}} = \frac{\int G(\theta,\phi)R(\theta,\phi)^{-4}\sigma(\theta,\phi,U)J(\theta,\phi)\mathrm{d}\theta\mathrm{d}\phi}{\int G(\theta,\phi)R(\theta,\phi)^{-4}J(\theta,\phi)\mathrm{d}\theta\mathrm{d}\phi}, \quad (3)$$

where J is the Jacobian of transform from $\{\mathbf{x}\}$- to $\{\theta,\phi\}$-coordinates.

To find the true NRCS, $\sigma(\theta,\phi,U)$, from measured NRCS the integral equation (3) is solved numerically by minimizing the norm of residuals between the measured NRCS and a fitting model, which is represented in a form of polynomial function (see e.g. (Ulaby et al., 1986; Wentz and Smith, 1999)):

$$\log(\sigma) = \sum_{m=0}^{4}\sum_{n=0}^{2}\sum_{k=0}^{1} C_{mnk}\theta^m \cos(n\phi)(\log U)^k, \quad (4)$$

where C_{mnk} are the coefficients (30 per each polarization) to be found from the fitting procedure.

Observed NRCS varies in a wide range from -40 dB to 15 dB, thus the minimization is performed for σ represented in logarithmic units. Since the number of measurements is of the order of 1000, the system of linear equations (4) is overdetermined. The true NRCS satisfies the non-linear integral equation (3), which is solved iteratively using the simplex direct search method (Lagarias et al., 1998) starting with the fitting model (4) for the measured NRCS as the first guess (shown in Figure 2 by solid lines). The final C_{mnk} values are given in Table 1.

The accuracy of the fitting method is checked by applying the antenna pattern to the solution (4) and comparing the result with the measured NRCS. The model root-mean-square errors are found to be 1.47 dB and 1.50 dB for VV and HH polarization, respectively, with 0.98 correlation coefficient.

Applicability limits for our empirical model (Ka-band Dual co-Polarized Model, KaDPM) are defined by the variety of observations and technical limitations of the radar. The reliable wind speed range is 3 m/s – 18 m/s. The fit at low incidence angles is less confident due to poor statistics, thus the KaDPM is valid for $25^\circ < \theta < 65^\circ$.

Table 1. Coefficients C_{mnk} for VV and HH polarizations (θ and φ are in degrees, U is in m/s).

m	n	k	VV	HH	m	n	k	VV	HH
0	0	0	3.206118e+0	3.287958e+0	0	0	1	-2.007813e-1	-1.435727e-1
1	0	0	3.406090e-2	5.163962e-4	1	0	1	-2.716294e-2	-2.817042e-2
2	0	0	-2.195761e-2	-2.001378e-2	2	0	1	5.420938e-3	5.395528e-3
3	0	0	4.560768e-4	4.135832e-4	3	0	1	-1.013182e-4	-1.084762e-4
4	0	0	-2.676594e-6	-2.451252e-6	4	0	1	5.034803e-7	6.285627e-7
0	1	0	-3.791021e-2	-6.110719e-2	0	1	1	2.754555e-2	2.209574e-2
1	1	0	7.319559e-2	5.390237e-2	1	1	1	-4.146333e-2	-3.469291e-2
2	1	0	-4.075472e-3	-3.379093e-3	2	1	1	2.142708e-3	2.091275e-3
3	1	0	5.950113e-5	5.879322e-5	3	1	1	-2.837956e-5	-3.386480e-5
4	1	0	-2.139149e-7	-2.230532e-7	4	1	1	8.711814e-8	1.361685e-7
0	2	0	1.123723e-2	3.093813e-2	0	2	1	-4.769737e-3	-4.955172e-3
1	2	0	1.361032e-1	1.132816e-1	1	2	1	-7.422097e-2	-6.289764e-2
2	2	0	-9.541387e-3	-9.608499e-3	2	2	1	5.920139e-3	5.855362e-3
3	2	0	2.491352e-4	2.604245e-4	3	2	1	-1.527474e-4	-1.544211e-4
4	2	0	-2.082505e-6	-2.181777e-6	4	2	1	1.234758e-6	1.236034e-6

3.2 Model of NRCS

The KaDPM is compared with published Ka-band data (Masuko et al., 1986; Giovanangeli et al., 1991; Plant et al., 1994) as well as with Ku-band co-polarized backscatter models (Wentz and Smith, 1999, NSCAT-4) and (Quilfen et al., 1999) (Figures 3,4,5).

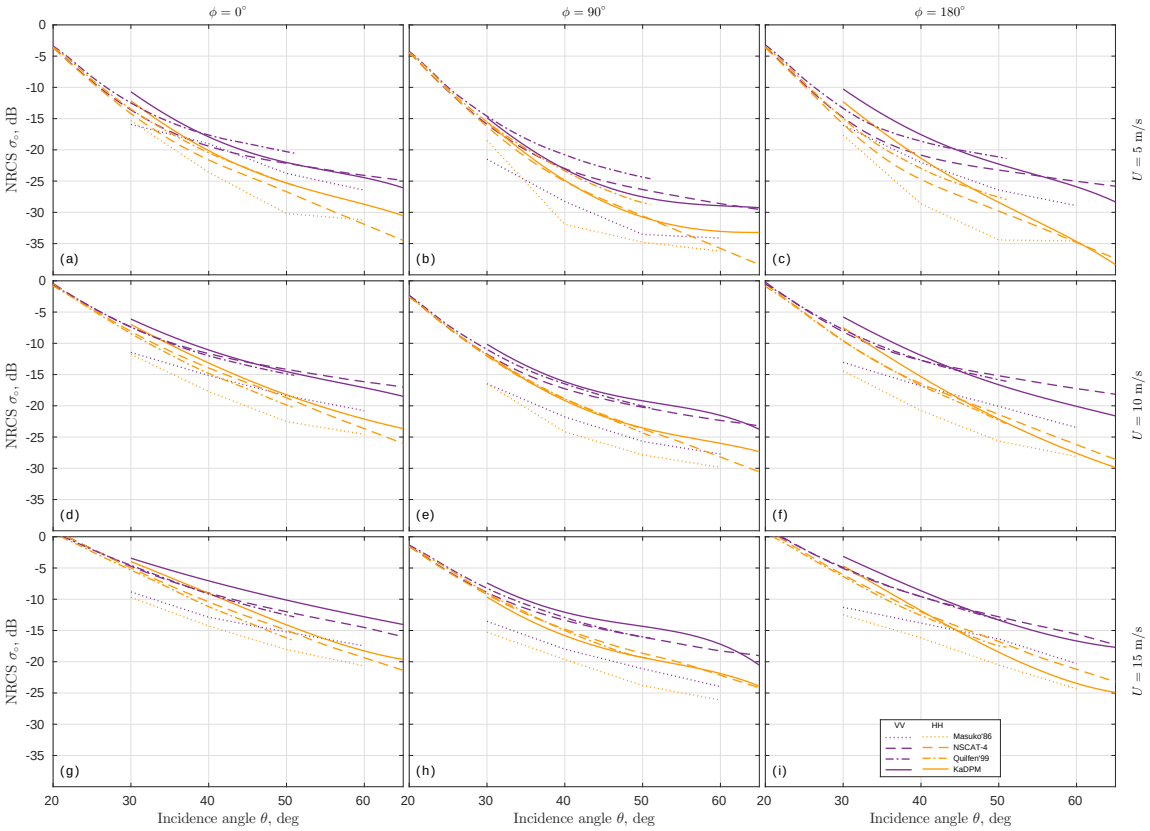

Figure 3. NRCS versus incidence angle: (left column) upwind, (middle column) crosswind, (right column) downwind directions at $U = 5$ m/s (top row), $U = 10$ m/s (middle row) $U = 15$ m/s (bottom row).

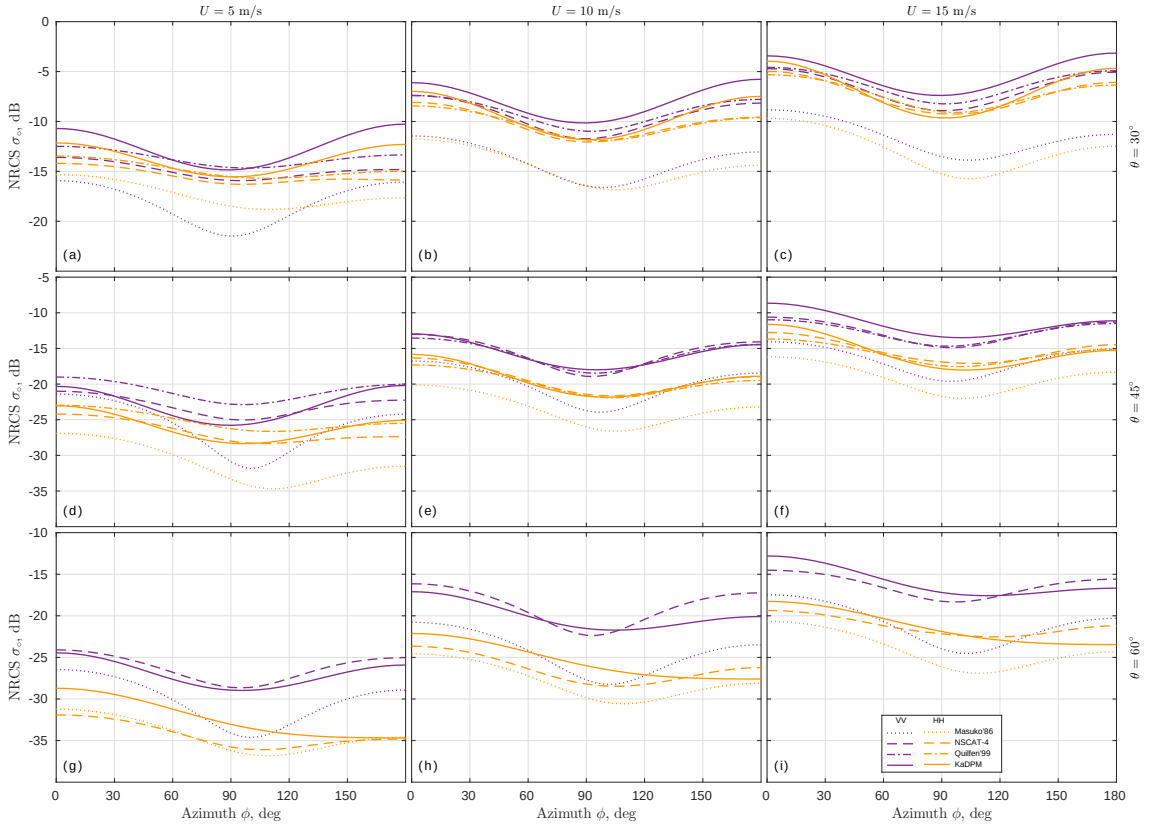

Figure 4. NRCS versus azimuth at wind speed 5 m/s (left column), 10 m/s (middle column) and 15 m/s (right column) at $\theta = 30^\circ$ (top row), $\theta = 45^\circ$ (middle row), $\theta = 60^\circ$ (bottom row).

In general, the KaDPM is systematically higher by 5-10 dB than (Masuko et al., 1986) as it was first discussed in (Walsh et al., 1998; Vandemark et al., 2004). But, the KaDPM agrees well with Plant's et al. (1994) data collected in near-upwind azimuths at $\theta = 45^\circ$ (Figure 5b). Giovanageli et al. (1991) laboratory VV measurements are available at $\theta = 30^\circ$ for all azimuths. The KaDPM is consistent with it in the upwind direction (Figure 5a), but is 2 – 4 dB lower in downwind and crosswind directions (Figure 5a).

Comparison of KaDPM with the Ku-band models reveals quite reasonable correspondence at high incidence angles, $\theta > 45^\circ$. However, the KaDPM may significantly exceed the Ku-band NRCS at lower incidence angles (Figure 3). In particular, the difference from the Ku-band reaches 5 dB at $\theta = 30^\circ$ and $U = 5$ m/s in the downwind direction (Figure 4a).

Azimuth distribution of the KaDPM demonstrates the features, which are similar to the measured NRCS (compare Figure 2 and 4). Both, KaDPM and Ku-band models have similar azimuth dependence at rather strong winds, $U > 10$ m/s. But at weaker winds, $U = 5$ m/s, the azimuth dependence of Ka-band NRCS becomes stronger than that in Ku-band.

At low incidence angles, $\theta < 30^\circ$, the upwind-downwind difference is near zero or negative (in dB, Figure 6a-c). At larger incidence angles, this difference grows up to more expected positive values, and even becomes stronger than in Ku-band for both polarizations.

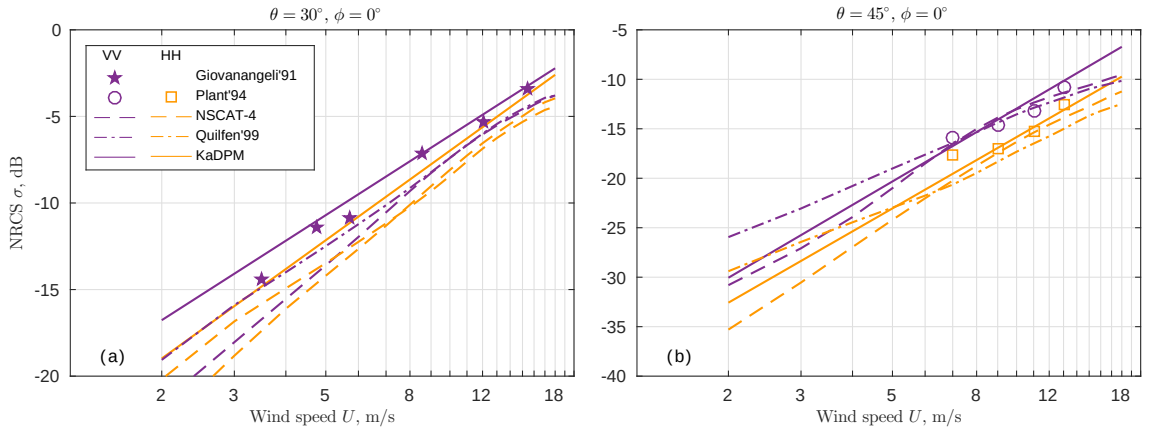

Figure 5. NRCS versus wind speed in upwind direction at (a) $\theta = 30^\circ$, (b) $\theta = 45^\circ$.

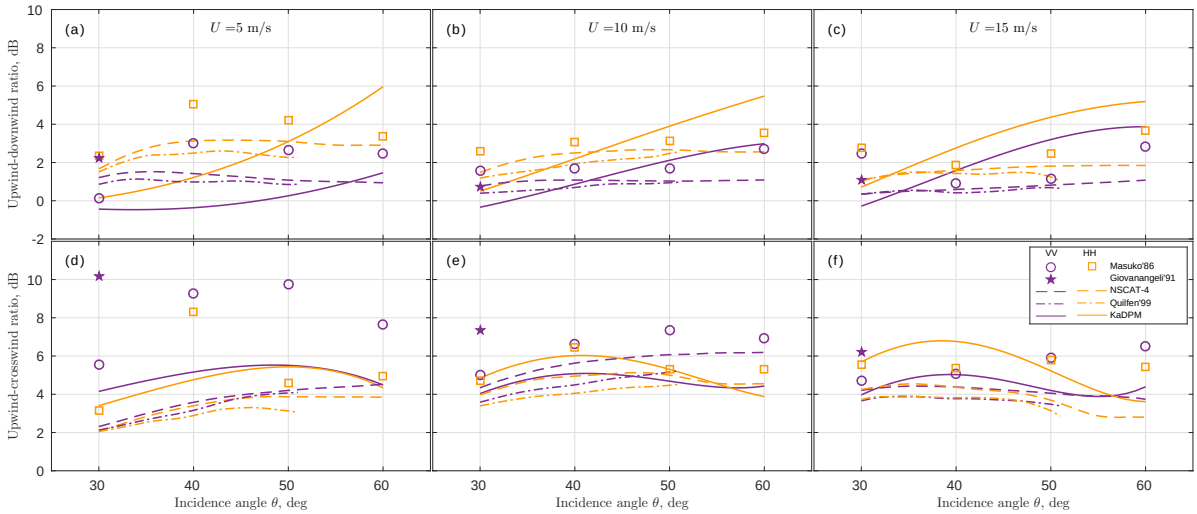

Figure 6. (a,b,c) NRCS upwind/downwind ratio and (d,e,f) NRCS crosswind/upwind ratio versus incidence angle at $U = 5$ m/s (left), $U = 10$ m/s (middle), $U = 15$ m/s (right column).

Generally, the Ka-band upwind-crosswind difference is similar to that in Ku-band. It has maximum values at moderate incidence angles, $40^\circ < \theta < 50^\circ$. However at large incidence angles ($\theta = 60^\circ$), the crosswind Ka-band HH polarization NRCS becomes lower than in the downwind direction that results in unimodal azimuth distribution (Figure 4 and 6). Except for the low winds, an overall consistency of upwind-downwind and upwind-crosswind asymmetry predicted by KaDPM and (Masuko et al. 1986) data is also noticeable.

3.3 Polarization Ratio and Difference

Following (Kudryavtsev et al., 2013) the NRCS is decomposed into a sum of polarized and non-polarized (NP) components, $\sigma^{pp} = \sigma^{pp}_{br} + \sigma_{np}$. The polarized term, σ^{pp}_{br}, is estimated using two-scale Bragg backscattering model (TSM), which suggests that σ^{VV}_{br} is always higher than σ^{HH}_{br} (Valenzuela, 1978; Kudryavtsev et al., 2004). The NP term is associated with quasi-specular reflections from regular surface and breaking waves. The polarization ratio (PR), σ^{VV}/σ^{HH}, is an indicator of different backscattering mechanism contribution. Depending on the relative NP contribution, the PR varies from 1 (if NP scattering dominates) to $P_{br} = \sigma^{VV}_{br}/\sigma^{HH}_{br}$ (if NP scattering is negligible).

Both the KaDPM and Ku-band GMF PR are lower than TSM PR indicating a non-negligible NP scattering (Figure 7a,b). Observed PR is closer to the Bragg TSM PR in the downwind direction where the NP scattering by breaking waves is minimal. At $\theta < 55^\circ$, the PR is minimal in the upwind direction suggesting that impact of the NP component is the strongest in this direction. At, $\theta > 55^\circ$ the maximal impact of NP shifts into the crosswind direction where the Bragg scattering is weak. In general, the Ka-band PR is qualitatively similar to Ku-band, except for $\theta > 45^\circ$, where Ka-band PR is lower due to stronger NP scattering by breaking waves.

The upwind and crosswind PR increases towards TSM PR with wind (Figure 7b). This suggests that capillary Bragg waves grow with wind faster than wave breaking responsible for NP scattering. This feature distinguishes remarkably Ka-band from Ku-band and C-band (Mouche et al., 2006), for which the relative role of the Bragg backscattering is weakening with wind.

The polarization difference (PD), $\sigma^{VV} - \sigma^{HH}$, does not include the NP backscattering, and thus it describes only the Bragg scattering characteristics. The Bragg waves (and thus PD) are strongly wind dependent (Figure 7c,d). Both, Ka- and Ku-band PD demonstrate strong wind directionality seen in its lower values in the crosswind direction. The KaDPM wind exponent in the upwind and downwind directions is about 2.5 and 2, respectively. The Ku-band wind exponent is about 2 in these two directions. In the crosswind direction, the KaDPM wind exponent (~3) exceeds its upwind and downwind values. This is in contrast to the Ku-band that has lower crosswind wind

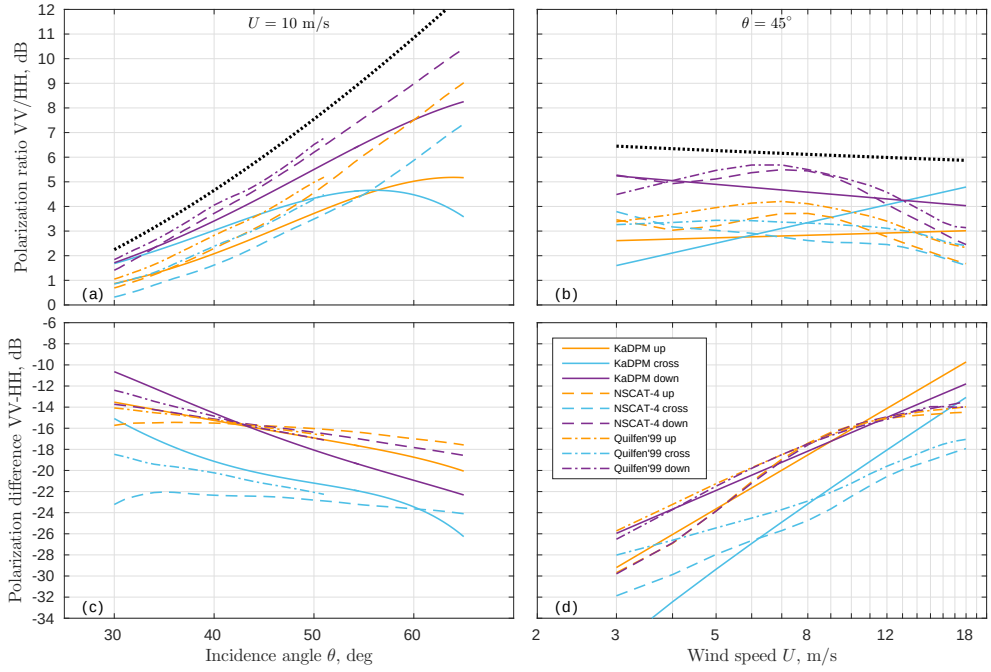

Figure 7. (a,b) Polarization ratio and (c,d) polarization difference versus (a,c) incidence angle at $U = 10$ m/s and (b,d) wind speed at $\theta = 45^\circ$ from KaDPM (solid lines), Ku-band (dashed and dash-dotted lines) and Bragg Two-Scale Model (black dotted lines).

exponent < 2.

The upwind-downwind asymmetry of PD has more complicated behavior. In the frame of the Bragg TSM, this asymmetry is attributed to the correlation of the Bragg wave energy with the tilting long wave slopes, which is positive/negative if Bragg roughness is enhanced on upwind/downwind slopes, respectively. The Ka- and Ku-band models suggest that both signs of upwind-downwind asymmetry are possible. In particular (Figure 7c), the downwind PD is larger than upwind PD at $\theta < 45^\circ$ for $U = 10$ m/s, and *vice versa* at larger incidence angles. At fixed $\theta = 45^\circ$, the Ka-band upwind-downwind PD asymmetry is wind dependent (Figure 7d). At $U = 10$ m/s, the KaDPM downwind PD is larger than upwind PD, but this asymmetry changes sign at stronger winds. However at $\theta = 45^\circ$, the Ku-band upwind and downwind PD are almost identical.

The presence of Ka-band PD maximum in the upwind direction at high winds and large incidence angles (Figure 7c,d) is expectable due to the effect of enhancement of the parasitic capillary (bound) waves on the forward slopes of the tilting waves. But, the origin of the downwind PD maximum, which is observed at lower winds and incidence angles in the Ka-band and Ku-band as well as in the C-band (Mouche and Chapron, 2015), is not clear. Possibly this is caused by the small scale roughness covering the backward slopes of breaking crests, which dominates the upwind-downwind asymmetry at low incidence angles, $\theta < 45^\circ$. At the larger incidence, the Bragg roughness (including parasitic capillaries) covering the forward breaking wave slope, which is steeper than backward, predominate the asymmetry.

4. SUMMARY

In this paper the field measurements of Ka-band backscattering cross-sections of the sea surface are presented. The experiments are conducted from the Black Sea Research platform during 2009 – 2015.The measured NRCS is corrected for the impact of the antenna angular pattern and presented in a form of empirical function as a conventional truncated Fourier series, which is valid for $25^\circ < \theta < 65^\circ$, $U < 18$ m/s (the KaDPM).

It is found that (Masuko et al., 1986) data are by 5 – 10 dB lower relative to the KaDPM that is attributed (after (Walsh et al., 1998)) to uncertainties in their data calibration. The KaDPM is consistent with independent Ka-band data collected in field (Plant et al., 1994) and laboratory (Giovanangeli et al., 1991) conditions. In general, the KaDPM is consistent with the empirical Ku-band GMFs (Wentz and Smith, 1999; Quilfen et al., 1999) in a wide range of wind speeds and incidence angles. However, some remarkable differences between Ku- and Ka-band are presented.

Unlike Ku-band, the Ka-band PR increases remarkably with wind towards TSM PR values. This suggests that Bragg waves grow with wind speed faster than NP backscattering component associated with wave breaking. The PD, and thus Ka-band Bragg waves, are strongly wind dependent, with wind exponent about 2.5 and 3 in the upwind and crosswind directions, respectively. That is consistent with optical measurements of wave spectra (Jähne and Riemer, 1990; Yurovskaya et al., 2013). The PD (capillary Bragg waves) is strongly anisotropic in azimuth with a minimum in the crosswind direction. Upwind-to-downwind asymmetry has more complicated behavior. At $\theta < 45^\circ$ and $U < 10$ m/s, the downwind PD exceeds the upwind PD, suggesting that Ka-band Bragg waves are enhanced on the windward slopes of long tilting waves. At larger incidence angles and stronger winds the PD maximum shifts in the upwind direction, what is anticipated if Bragg waves are mainly generated as micro-scale wave breaking and parasitic capillaries.

ACKNOWLEDGMENT

The work has been supported by the Russian Ministry of Education and Science under project no. RFMEFI57714X0056, and by NASA/Physical Oceanography grant NNX15AG40G.

REFERENCES

Boisot, O., S. Pioch, C. Fatras, G. Caulliez, A. Bringer, P. Borderies, J.-C. Lalaurie, and C.-A. Guérin, 2015. Ka-band backscattering from water surface at small incidence: A wind-wave tank study. Journal of Geophysical Research (Oceans), 120, pp. 3261–3285.

Doerry, A. W., D. F. Dubbert, M. Thompson, and V. D. Gutierrez, 2005. A portfolio of fine resolution Ka-band SAR images: part I. In: Radar Sensor Technology IX, Society of Photo-Optical Instrumentation Engineers (SPIE) Conference Series, edited by R. N. Trebits and J. L. Kurtz, 5788, pp. 13–24.

Durand, M., Lee-Lueng Fu, D. P. Lettenmaier, D. E. Alsdorf, E. Rodriguez, and D. Esteban-Fernandez, 2010. The surface water and ocean topography mission: Observing terrestrial surface water and oceanic submesoscale eddies. Proceedings of the IEEE, 98(5), pp. 766–779.

Fairall, C. W., E. F. Bradley, J. E. Hare, A. A. Grachev, and J. B. Edson, 2003. Bulk Parameterization of Air Sea Fluxes: Updates and Verification for the COARE Algorithm. Journal of Climate, 16, pp. 571–591.

Giovanangeli, J.-P., L. F. Bliven, and O. Le Calve, 1991. A wind-wave tank study of the azimuthal response of a Ka-band scatterometer. IEEE Transactions on Geoscience and Remote Sensing, 29, pp. 143–148.

Jähne, B., and K. S. Riemer, 1990. Two-dimensional wave number spectra of small-scale water surface waves. Journal of Geophysical Research (Oceans), 95(C7), pp. 11531–11546.

Kudryavtsev, V. N., B. Chapron, A. G. Myasoedov, F. Collard, and J. A. Johannessen, 2013. On Dual Co-Polarized SAR Measurements of the Ocean Surface. IEEE Geoscience and Remote Sensing Letters, 10, pp. 761–765.

Kudryavtsev, V. N., D. Hauser, G. Caudal, and B. Chapron, 2003. A semiempirical model of the normalized radar cross-section of the sea surface 1. Background model. Journal of Geophysical Research (Oceans), 108(C3), pp. FET 2–1–FET 2–24.

Lagarias, J. C., J. A. Reeds, M. H. Wright, and P. E. Wright, 1998. Convergence Properties of the Nelder-Mead Simplex Method in Low Dimensions. SIAM Journal of Optimization, 9(1), pp. 112–147.

Masuko, H., K. Okamoto, M. Shimada, and S. Niwa, 1986. Measurement of microwave backscattering signatures of the ocean surface using X band and K$_a$ band airborne scatterometers. Journal of Geophysical Research (Oceans), 91, pp. 13,065–13,084.

Mouche, A., and B. Chapron, 2015. Global C-band Envisat, Radarsat-2 and Sentinel-1 SAR measurements in copolarization and cross-polarization. Journal of Geophysical Research: Oceans, doi:10.1002/2015JC011149.

Mouche, A. A., D. Hauser, and V. Kudryavtsev, 2006. Radar scattering of the ocean surface and sea-roughness properties: A combined analysis from dual-polarizations airborne radar observations and models in C band. Journal of Geophysical Research (Oceans), 111(C10), doi:10.1029/2005JC003166.

Nekrasov, A., and P. Hoogeboom, 2005. A Ka-Band Backscatter Model Function and an Algorithm for Measurement of the Wind Vector Over the Sea Surface. IEEE Geoscience and Remote Sensing Letters, 2, pp. 23–27.

Plant, W. J., E. A. Terray, R. A. Petitt, and W. C. Keller, 1994. The dependence of microwave backscatter from the sea on illuminated area: Correlation times and lengths. Journal of Geophysical Research (Oceans), 99, pp. 9705–9723.

Quilfen, Y., B. Chapron, A. Bentamy, J. Gourrion, T. El Fouhaily, and D. Vandemark, 1999. Global ERS 1 and 2 and NSCAT observations: Upwind/crosswind and upwind/downwind measurements. Journal of Geophysical Research (Oceans), 104(C5), pp. 11459–11469.

Tanelli, S., S. L. Durden, and E. Im, 2006. Simultaneous Measurements of Ku- and Ka-Band Sea Surface Cross Sections by an Airborne Radar. IEEE Geoscience and Remote Sensing Letters, 3, pp. 359–363.

Ulaby, F. T., R. K. Moore, and A. K. Fung, 1986. Microwave Remote Sensing: Active and Passive., 3, pp. 1065–2126, Artech House, Dedham, USA.

Vandemark, D., B. Chapron, J. Sun, G. H. Crescenti, and H. C. Graber, 2004. Ocean Wave Slope Observations Using Radar Backscatter and Laser Altimeters. Journal of Physical Oceanography, 34, pp. 2825–2842.

Valenzuela, G. R., 1978. Theories for the interaction of electromagnetic and ocean waves - a review. Boundary Layer Meteorology, 13, pp. 61–85.

Vincent, P., N. Steunou, E. Caubet, L. Phalippou, L. Rey, E. Thouvenot, and J. Verron, 2006. AltiKa: a Ka-band Altimetry Payload and System for Operational Altimetry during the GMES Period. Sensors, 6(3), pp. 208–234.

Walsh, E. J., D. C. Vandemark, C. A. Friehe, S. P. Burns, D. Khelif, R. N. Swift, and J. F. Scott, 1998. Measuring sea surface mean square slope with a 36-GHz scanning radar altimeter. Journal of Geophysical Research (Oceans), 103(C6), pp. 12587–12601.

Wentz, F. J., and D. K. Smith, 1999. A model function for the ocean-normalized radar cross section at 14 GHz derived from NSCAT observations, Journal of Geophysical Research (Oceans), 104(C5), pp. 11499–11514.

Yurovskaya, M. V., V. A. Dulov, B. Chapron, and V. N. Kudryavtsev, 2013. Directional short wind wave spectra derived from the sea surface photography. Journal of Geophysical Research (Oceans), 118, pp. 4380–4394.